Non-Gaussianity in the CMB: Directional analysis and application of needlets

Øystein Rudjord

INSTITUTE OF THEORETICAL ASTROPHYSICS
UNIVERSITY OF OSLO

APRIL 2010

Series of dissertations submitted to the
Faculty of Mathematics and Natural Sciences, University of Oslo
No. 977

ISSN 1501-7710

Cover: Inger Sandved Anfinsen.
Printed in Norway: AiT e-dit AS.

Produced in co-operation with Unipub.
The thesis is produced by Unipub merely in connection with the
thesis defence. Kindly direct all inquiries regarding the thesis to the copyright
holder or the unit which grants the doctorate.

Acknowledgements

This thesis would never have seen the light of day if it was not for the guidance and support from a number of people.

First of all I would like to express my sincere gratitude to my supervisor Frode Hansen who has guided me through these four turbulent years with endless patience and enthusiasm. He has always been available for discussions and directed me with the right questions. His curiosity towards research and keen intuition has always been a source of inspiration.

During my PhD studies I also had the pleasure to work with Hans Kristian Eriksen. I am grateful to him for for introducing me to new topics and always finding time to answer my countless questions. I also wish to thank Domenico Marinucci for fruitful collaboration.

Additionally I would like to thank all the people at the institute who have contributed to make these years an excellent time, both scientifically and socially. In particular I am thankful to my office mates, Nicolaas, Magnus and Kristin for contributing to a cheerful and stimulating work environment.

And last but not least I am grateful to Zofia and my family for their support and encouragement.

Contents

Part I

Introduction

Chapter 1

Cosmology and CMB

1.1 Introduction

The field of cosmology today is very dynamic. Our understanding of the universe is constantly maturing at a rapid pace. Before approaching the main topics of this thesis, I would like to present a brief overview of the current status of cosmology, how the universe was understood when this thesis was written [1].

1.1.1 Cosmology

Cosmology is the science about the universe we live in on the very largest scales. It encompasses the history, the contents and the future of our universe. By today it describes a universe which was once a hot dense fog placed in a space which expanded like a stretched rubber sheet. And somehow as it expanded and cooled down it developed a rich structure with stars and galaxies and people.

The big bang theory has become fundamental in our understanding of the universe. It forms the baseline of all current cosmological models. This theory basically states that the universe is expanding. It has been expanding for quite a while (around 14 billion years according to current estimates [Bennett et al. 2003a]). This means that the universe at earlier times must have been more dense, and therefore also hotter. And in the very early universe, it must have been very hot and dense. Turning this around, we say that the universe originated in a very hot and dense state, and then expanded to the size it is today. During this expansion the universe gradually cooled down and areas with higher density than the surroundings collapsed and formed galaxies and stars.

If we continue to extrapolate backwards in time we will at some point reach a hypothetical state where the universe is infinitely dense. This is the point which we refer to as the big bang event. This is not really a part of the big bang theory. As the density approaches infinity, the laws of physics as we know them break down.

[1] For a more detailed introduction to cosmology, the reader is referred to [Dodelson 2003].

The singularity itself it therefore an invalid extrapolation of our theories. However, we still use it as a reference point for time when talking about the early universe.

The standard model of cosmology within the big bang framework is called the ΛCDM model. It describes the composition and the details of the evolution of the universe. It is the simplest model which is in general agreement with observations.

The dynamics of the expansion is closely coupled to the contents of the universe. Within the ΛCDM model, the universe contains three basic components: matter, radiation and dark energy. The composition of these have varied through time, and they have all played their part in shaping the history of the universe.

The most familiar component is the one which we call *matter*. It makes up for around 30% of the energy contents of the universe. Only around a fifth of this however, is baryonic matter, which make up the atoms and thereby everything we see around us.

Most of the matter in the universe seems to be of a different nature. The cold dark matter (CDM) is a mysterious substance which does not interact electromagnetically. This means that we can not see it directly, only measure the gravitational effects on its surroundings. We do not know what the cold dark matter is made of. There exist several possibilities, but they all extend beyond the standard model of particle physics today (see for example [Bertone et al. 2005]).

The second basic component of the universe is *radiation*. Today this make up for just a tiny fraction of the contents of the universe. However, at earlier times (the first ~ 70000 years after the big bang) radiation was the dominating energy component, and it played an important role in the evolution of the universe.

The remaining $\sim 70\%$ of the energy contents of the universe is *dark energy*. This is maybe the biggest unsolved problem of cosmology today, since we simply do not know what it is. We only observe the effect it has on the expansion of the universe. Without this component, we would expect the expansion to gradually slow down, and possibly at some point the universe would start to contract. This could happen since the gravitational force of all the contents of the universe would pull it together. However, when we try to measure the recent expansion history, we find that the expansion is not slowing down, it is accelerating [Perlmutter et al. 1999].

There are many models trying to explain this acceleration, often by either introducing a new type of cosmic fluid, or by modifying gravity. The hypothetical component that causes this acceleration, is what we call dark energy. Whatever it is, it is not like anything we have seen before.

Although these basic components contain several unknowns, they are capable of describing the expansion and composition of the universe from early times until today, and explain the large scale observations with a remarkable precision.

1.1.2 Inflation

The scenario in the previous section is unfortunately not enough to fully explain the universe we live in today. For some time there were a few unresolved questions

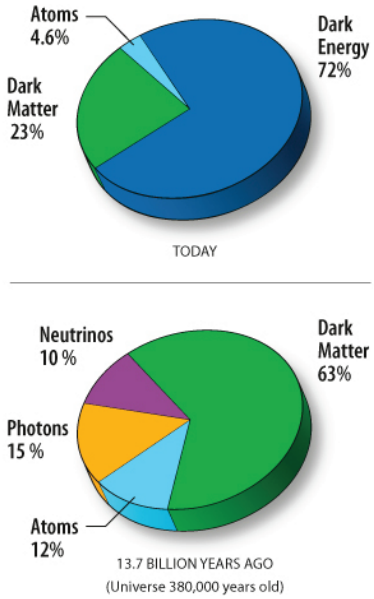

Figure 1.1: The composition of the universe, today and at recombination, $\sim$ 400000 years after big bang. (Image: NASA / WMAP Science Team)

in cosmology.

The flatness problem The geometry of the universe is remarkably flat. What makes this strange is that earlier, it must have been even flatter. Any curvature would have increased throughout the evolution of the universe. This means that the universe must have started out as extremely flat. And this precise fine-tuning of the curvature deserves an explanation.

The horizon problem When we study the cosmic microwave background (CMB) –a relic radiation from the early universe that will be properly introduced in the next section– we find that it keeps almost the same temperature in all directions. The relative temperature variations on the sky are only $\sim 10^{-5}$. This is quite strange given that two points in opposite directions on the last scattering surface (the apparent surface, from which the CMB is released) should never have been in causal contact before, according to the expected expansion history. Yet, the homogeneity in the temperature indicates that these two distant points have at some time been in thermal contact.

The monopole problem The early universe must have been very hot and dense. At some point it must have been so hot that our standard model of particle physics was not valid, and we may have to use a (yet uncovered) grand unified theory (GUT) to describe the particle interactions. However, as the universe expanded and cooled down several symmetries would have been broken before we were left with the standard model physics we know today. But during such a symmetry breaking field theory predict the production of magnetic monopoles, and for most GUT's it predicts a lot of them. Enough to dominate the universe. However, so far not a single monopole has been found.

The primordial seeds The model for the universe that we have discussed so far assumes a completely homogeneous universe. Our observations show that this is a good assumptions on very large scales. However, we know that on relatively small scales the universe is far from homogeneous. We have a lot of structures like stars, galaxies and clusters. Assuming that we had some small density perturbations in the early universe, gravity would make them grow, and later collapse to the structures we see today. But we need some physical mechanism to describe how these perturbations arose in the first place.

There is a way to solve all these problems at once. In 1981 Alan Guth [Guth et al (1981)] proposed that an epoch in the very early universe (around $\sim 10^{-34}$s after the big bang) with extremely rapid expansion could explain these phenomena. Today this expansion is usually explained by introducing of one or more fundamental fields. This epoch of rapid expansion is called inflation, and the field responsible for it is usually referred to as the inflaton.

However, even though inflation is commonly accepted as a likely explanation for the problems mentioned above, there exist many different models for inflation (see for example [Bartolo et al. 2004]). The most popular one is called single-field slow roll inflation. In this model inflation is driven by a scalar field which is "rolling" very slowly down a potential.

An epoch of inflation would explain the flat early universe, since the extreme expansion would smooth out any curvature. It would also explain the thermal contact of distant points (the horizon problem). Two points that were in contact before inflation, could easily end up separated by distances larger than today's causal horizon. When they now enter the horizon again, we see two distant points that once were very close, and therefore has almost the same temperature.

The missing monopoles are also no longer a problem. There might have been a lot of monopoles before inflation, but after the extreme expansion these would be spread out very thin. With today's models of inflation we would expect only a single monopole in the observable universe.

Inflation is also capable of explaining the primordial seeds for structure formation. Small quantum fluctuations in the inflaton field during inflation would have expanded to cosmological scales. These would then be large enough to start contracting because of gravity. This means the structures we see today originated as quantum fluctuations. In this way, the physics of the largest scales meets the physics of the smallest scales.

1.1.3 The Cosmic Microwave Background

When we observe astrophysical objects, we are looking back in time. Since light travels with a finite speed, everything we see is from the past. For close objects the time difference is small, and is less significant (For example, it takes 8 minutes for light to travel to the earth from the sun.). However, for more distant objects, the light may have travelled for millions, or even billions of years. In these cases we are really seeing how the objects looked millions of years ago. In a way we are seeing an older and older universe the further away we look. This is of course very convenient for cosmologists, who are terribly curious about the early universe. The oldest object we can observe in the universe today is the Cosmic Microwave Background (CMB) radiation, appearing as a very faintly glowing fog, around 13 billion light years away.

To see where this radiation comes from, we have to look back at the early universe, around 400000 years after the big bang. At this time the universe was filled with a hot fog of protons, electrons and photons. The temperature was too high for the particles to bind, and form neutral atoms. The fog therefore consisted of charged particles which had a high probability of interacting with the photons. For this reason, the photons were never able to travel long distances undisturbed. They bounced around between the protons and electrons, resulting in an opaque universe.

As the early universe expanded, it gradually cooled down. At some point it

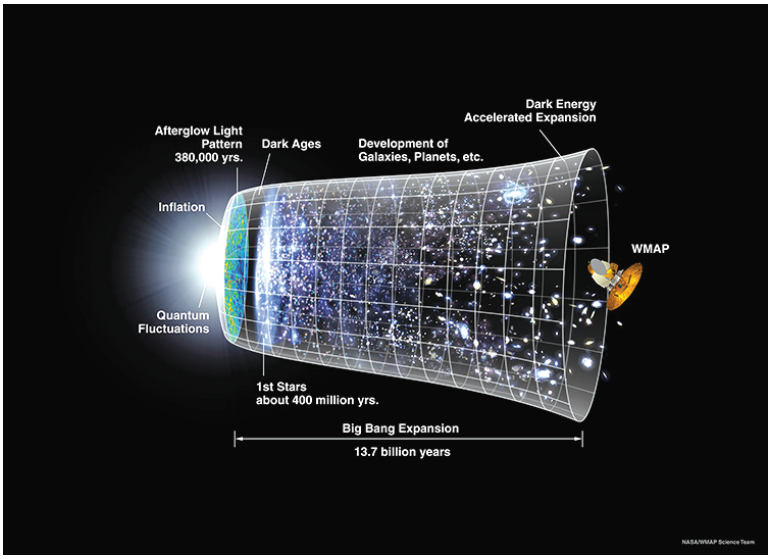

Figure 1.2: The evolution of the universe. To the far left we see very rapid expansion, due to inflation. Just after inflation (approx. 400000 years later) is the cosmic microwave background radiation, the earliest part we can observe. Note the slightly accelerated expansion at later times, due to dark energy. (Image: NASA / WMAP Science Team)

became cold enough for electrons and protons to form atoms. The fog was now electrically neutral, and no longer interfering with the photons. The universe had suddenly become transparent. As a result, photons were released from all over the universe, and were now able to travel undisturbed. This important event in the history of the universe is called recombination.

Today these photons are still around. Most of the radiation has travelled uninterrupted since it was released. The first people to detect it were Arno Penzias and Robert Wilson in 1965, who discovered a background signal while working on a new type of antenna ("the horn antenna"). To begin with they were not able to explain this signal, and thought something was wrong with the equipment. Only later, after communicating with the cosmological community it became clear that they were the first people to observe the relic radiation from big bang.

Since this radiation was the most important evidence for the big bang theory, many groups put an effort into measuring the temperature of the CMB. Later, in 1989 the satellite COsmic Background Explorer (COBE) was launched, carrying several instruments, one of them, Far Infrared Absolute Spectrophotometer (FIRAS) measured the spectrum of the CMB more precisely than ever before, and established that the CMB fits nearly perfectly to the Planck curve of black body radiation with temperature 2.7K [Mather et al. 1994]. This fits extremely well with the predictions of the big bang theory.

But the story does not end here. As mentioned in the previous section, inflation created small fluctuations in the gravitational potential by enlarging small quantum fluctuations. By the time of recombination these fluctuations had grown, due to the pull of gravity. This had led to local variations in the density of the fog. When the radiation was released, these density variations were imprinted in the CMB. If we measure the CMB temperature very precisely in different directions, we find tiny anisotropies corresponding to these density variations.

For this purpose, the COBE satellite also carried a Differential Microwave Radiometer (DMR). This instrument measured the variations in the CMB temperature on the sky [Bennett et al. 1996]. The resulting map of anisotropies is an image of the density variations in the early universe. And these density variations originated as quantum fluctuations during inflation. Thus, by studying the anisotropies of the CMB, we are studying the origin of the structure of the universe.

Through the CMB we have a unique possibility to study the early universe. Compared to most other types of observable structures, the fluctuations of the CMB are to a large extent unchanged since it was released. They have been only marginally affected by the evolution of the universe in general. What is more, the CMB has shown to contain a lot of information. Through CMB we are able to pin down all the cosmological parameters with higher precision than ever before [Larson et al. 2010].

The most recent full sky CMB data set comes from the Wilkinson Microwave Anisotropy Probe (WMAP) satellite experiment, by NASA [Bennett et al. 2003a, Hinshaw et al. 2009]. They have provided the community with publicly available full sky CMB maps. These are the data that will be studied in this thesis.

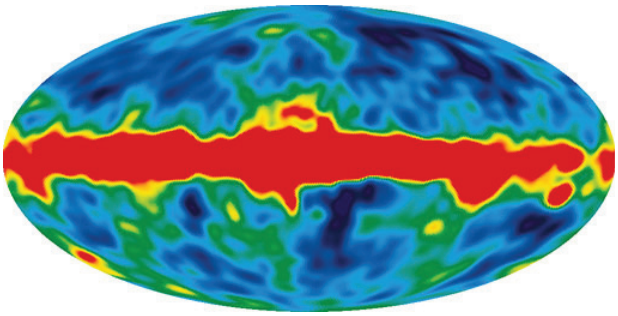

Figure 1.3: The map of the CMB temperature anisotropies on the sky as measured by the COBE DMR instrument. These show the density fluctuations at recombination. The temperature fluctuations on this maps are within $\pm 100 \mu K$. (The figure is taken from *http://lambda.gsfc.nasa.gov*)

1.2 Working with CMB Data

1.2.1 Data reduction and analysis

Although building an instrument for measuring the tiny CMB anisotropies, is quite an achievement by itself, there is still work to do before we can extract information about cosmology from them. We need to make a map of the anisotropies, and understand its properties and limitations, before we use it to constrain cosmological parameters.

Methods

The data we receive from the instrument are called the time-ordered data. This is a long stream of numbers encoding the temperature in the direction the instrument was pointing at a given time. For most practical purposes however, we need a map of the CMB sky. The somewhat challenging task of assembling a map of the sky from this, is what we call map making.

During this process the map's beam and noise properties are found. These are important when we later want to simulate CMB sky maps. The CMB instrument has a finite resolution. This results in a smoothing of the features in the map, removing small scales. This smoothing can be represented by a beam function, which describes the damping of structures at different scales.

The instrument also leaves noise in the data. We can describe the noise as random values that are added to each pixel. For the WMAP data, the noise is assumed to be "white", meaning that it has the same properties on all scales. We can assume that the noise in the different pixels are uncorrelated. Because of the scanning strategy of the satellite, some areas of the sky are scanned more than

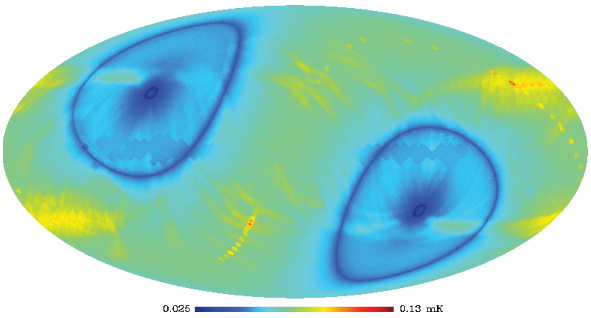

Figure 1.4: The root-mean-square of the noise for the V channel of the WMAP 5-year data. We can see how the satellite have been scanning the sky. The blue areas of around the ecliptic poles have less noise since it has been scanned more than the rest of the sky.

others, and thus have less noise. The noise is therefore represented by a Gaussian distribution with a root-mean-square described by the scanning. Figure 1.4 depicts the variation of the noise properties on the sky as a result of the scanning.

The noise influences the data very little on large scales. However, on smaller scales the contribution from the noise increases rapidly. This, in combination with the instrumental beam makes it difficult to extract information from the smallest scales where the signal is weak and the noise is dominating the data.

By now we have a raw map of the CMB sky, with known beam and noise properties. A map from one of the WMAP channels are shown in figure 1.5. But if we look at this map, we can see that there is a strong signal in the equatorial region of this map. This is radiation from the Milky Way, usually referred to as foregrounds. There are mainly three different foreground components polluting the map:

Free-free When charged particles collide, they emit radiation as they accelerate in each others electromagnetic field (Bremsstrahlung). In the Milky Way this radiation mainly comes from ionized hydrogen.

Synchrotron Electrons accelerated in the galaxy's magnetic field emit radiation.

Thermal dust In the milky way there are lots of dust. This dust is heated by radiation from the surrounding stars, and then emits thermal radiation.

In order to study the underlying microwave background, these foregrounds have to be removed as accurately as possible. There exist several methods for doing this, and unfortunately none of them are perfect. The key element of these methods is that the intensity of the foregrounds vary with the frequency, while the CMB is independent of frequency. The different foreground components are dominating at

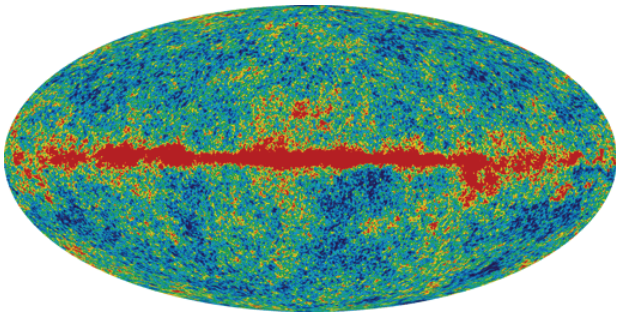

Figure 1.5: The raw map of the CMB anisotropies (V channel) on the sky as measured by the WMAP instrument. (The image is taken from *http://lambda.gsfc.nasa.gov*)

different frequencies. The intensity of the components can roughly be modelled as $\sim \nu^{\alpha}$ where ν is the frequency and α is a constant which is different for the three types of foregrounds [Bennett et al. 2003b]. Free-free and synchrotron radiation are most significant at low frequencies, with an decreasing emissivity at higher frequencies (although decreasing at different rates), while thermal dust dominates at higher frequencies. By combining CMB maps measured in different frequencies, it is possible to identify the foregrounds, and extract the constant, underlying microwave background radiation.

An example of a foreground cleaned map is given in figure 1.6. As we see, there are still foregrounds left in the galactic region. In addition to the foreground components from the milky way described above, it is also contains a number of point sources. These are bright galaxies appearing as bright dots on the map, covering one or a few pixels each. Since we do not want these to bias our analysis, we apply a mask, excluding the both the galactic region and ~ 1000 known point sources.

By now we have a map which should in principle be clean from foregrounds, and which we can use to estimate cosmological parameters. There are still a few steps we may take to simplify the data. The CMB map can be decomposed into spherical harmonic functions:

$$T(\theta,\phi) = \sum_{\ell} \sum_{m=-\ell}^{\ell} a_{\ell m} Y_{\ell m}(\theta,\phi) \tag{1.1}$$

where the spherical harmonic coefficients are given as

$$a_{\ell m} = \int Y^{*}_{\ell m}(\theta,\phi) T(\theta,\phi) \mathrm{d}\Omega \tag{1.2}$$

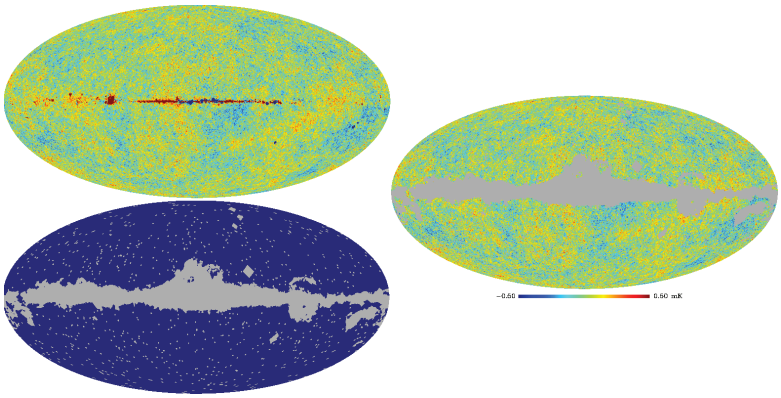

Figure 1.6: (*upper left*) The cleaned map of the CMB anisotropies (V channel) on the sky as measured by the WMAP instrument (5 year data). Note that there are still foregrounds left in the map. (*right*) The same map, but multiplied with the KQ85 mask from the WMAP 5-year release (*lower left*). This masks out the remaining foregrounds in the galactic region and ~ 1000 known point sources.

Now we may find the CMB power spectrum which describes the amplitude of the fluctuations on the various scales:

$$C_\ell = \frac{1}{2\ell+1}\sum_m a^*_{\ell m} a_{\ell m} \tag{1.3}$$

where the index ℓ indicates the scale. Larger ℓ represents smaller scales. The monopole ($\ell = 0$) is just the average temperature of the CMB. As the earth moves with respect to the background CMB, the radiation we measure is strongly redshifted in one direction and blueshifted in the other, creating a dipole ($\ell = 1$) which dominates the map. The true dipole of the CMB is practically impossible to find. Therefore, we usually remove the monopole and the dipole from the analysis and only consider multipoles $\ell \geq 2$. The power spectrum as measured by WMAP is shown in figure 1.7.

If we assume that the CMB fluctuations are Gaussian and isotropic as expected from single field slow roll inflation[2], then all the cosmological information of the CMB is contained in the power spectrum:

$$\langle a_{\ell m} a_{\ell' m'} \rangle = \langle C_\ell \rangle \delta_{\ell\ell'} \delta_{mm'}.$$

The brackets $\langle\rangle$ here indicates a mean taken from an ensemble of hypothetical realizations of our universe.

[2]Almost. Single field slow roll inflation predicts very small deviations from Gaussianity. [Maldacena (2003)]

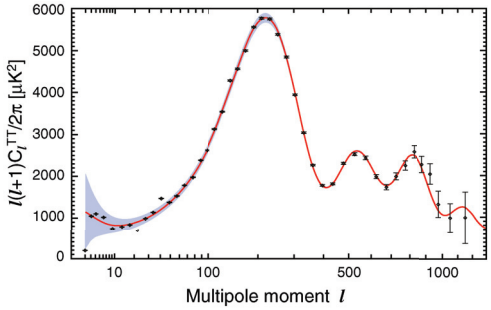

Figure 1.7: The WMAP 7-year best fit power spectrum (for ΛCDM) together with the power spectrum from the CMB (dots with error bars). This shows the amplitude of the fluctuations on different scales. The shaded region shows the cosmic variance. (The figure is taken from *http://lambda.gsfc.nasa.gov*)

It is of course a significant advantage to have all cosmological information condensed into a power spectrum containing $\sim 10^3$ numbers, as opposed to a full sky map, containing 10^6 numbers. The shape of the power spectrum depends on all the cosmological parameters, and therefore, this function alone can be used to estimate the full set of parameters.

A note of caution

The described procedure gives us estimates of the cosmological parameters with remarkable precision. This method does however come with a few assumptions:

Systematics We assumed that we have complete control over systematic effects. The noise was assumed to be white and with no correlations between the pixels. We assumed that the instrumental beam was symmetric, so we could express it as a simple beam function.

Foregrounds We cleaned the map from foregrounds and we assumed that there are none left in the data. Neither galactic nor point sources.

Gaussianity & Isotropy We assumed that the CMB was Gaussian and statistically isotropic.

Although these are widely used assumptions, their validity are debated. In this thesis we investigate the possibility of deviations from Gaussianity in the CMB. However, systematics and residual foregrounds are likely to also show up as non-Gaussian effects.

1.2.2 Gaussian simulations

As described in the previous section, we could condense all the cosmological information of the CMB into a power spectrum, which could be used to estimate all the cosmological parameters. It is also possible to go backwards. Given a set of cosmological parameters is is possible to find the theoretically predicted CMB angular power spectrum (For this purpose, we may use a Boltzmann code, for example CAMB[3]). Since this power spectrum contains all cosmological information of the CMB, we may use this to simulate Gaussian and isotropic realizations of the CMB sky.

When we say that the CMB is Gaussian, it means that the spherical harmonic coefficients, $a_{\ell m}$ are following a Gaussian distribution. Since we assume that the CMB is isotropic, the distribution is only dependent on the scale, ℓ (and not on the m index). As we saw from eq. 1.3, the variance of the $a_{\ell m}$'s are given by C_ℓ. The probability distribution of the spherical harmonic coefficients can then be written:

$$P(a_{\ell m}) = \frac{1}{\sqrt{2\pi\langle C_\ell\rangle}} e^{\frac{-a_{\ell m}^2}{2\langle C_\ell\rangle}} \tag{1.4}$$

where $\langle C_\ell\rangle$ is the theoretically predicted power spectrum.

Provided a power spectrum it is then relatively straightforward to simulate a set of Gaussian $a_{\ell m}$'s

$$a_{\ell m} = \varepsilon\sqrt{\langle C_\ell\rangle}$$

where ε is a variable drawn from a Gaussian distribution with zero mean and a standard deviation $\sigma = 1$. These $a_{\ell m}$ coefficients may then be transformed to a pixelized map using eq. 1.1. In this thesis I have used the HEALPix[4] package for making these simulations [Górski et al. 2005].

However, in order to have a complete simulation of the data, we must also include properties introduced to the data set by the instrument. As described earlier, the instrumental beam smoothes the map, reducing the amplitude of the small scales. This may be described by convolving the $a_{\ell m}$ coefficients with a beam function, B_ℓ:

$$a_{\ell m}^{smooth} = B_\ell a_{\ell m}$$

Often the beam function may be described as a Gaussian function. However, the instrumental beam of the WMAP data is highly non-Gaussian, and the beam function is provided by the WMAP team along with the data maps.

The noise properties of the instrument are also released along with the data. The noise may be simulated by adding a Gaussian random value to each pixel in the map.

$$T_i^{noisy} = T_i + \varepsilon N_i$$

[3] http://camb.info

[4] http://healpix.jpl.nasa.gov

where ε again represents a variable drawn from a Gaussian distribution of zero mean and $\sigma = 1$. The map N_i is the root-mean-square (RMS) of the noise, describing the noise level in different directions. An example of an RMS-map for the noise of the V channel of the WMAP data was shown in figure 1.4.

1.2.3 Experiments

We have already mentioned the COBE satellite which performed the first full-sky measurement of the CMB sky in the 1990's. Now it is time to introduce the two current full-sky CMB experiments, WMAP and Planck. For the work presented in this thesis, only the WMAP data has been used. However throughout the work, the Planck mission has always been hovering in the horizon, as the future ultimate CMB experiment.

WMAP

The Wilkinson Microwave Anisotropy Probe (WMAP) mission by NASA [Bennett et al. 2003a, Hinshaw et al. 2009] has provided us with the best publicly available full-sky maps of the CMB to date. The WMAP satellite was launched in 2001 and was expected to run for eight years. During the work presented in this thesis, the data release after five years of running was the best full-sky CMB data set available, and the one which has been used for the papers included. However, as this introduction is being written, a seven year data set has recently been released.

The WMAP instrument consists of 20 differential radiometers, covering 5 frequencies: 23 GHz (K channel), 33 GHz (Ka channel), 41 GHz (Q channel), 61 GHz (V channel) and 94 GHz (W channel). These provides full-sky maps with a angular resolution of $0.23^\circ - 0.93^\circ$ FWHM. The monopole is simply not measured (the instrument only measures differences in sky temperatures) and the dipole is removed since it is dominated by the redshift/blueshift caused by us (the satellite, the earth, the solar system and the galaxy) moving with respect to the last scattering surface.

The five maps which are produced have widely different properties because of their frequency ranges. For the work presented in this thesis only the Q, V and W channels are used, since the K and Ka channels are considerably more contaminated by foregrounds. This is likely to show up as non-Gaussian signals, and would interfere with the results.

For the three higher frequency channels, the noise increases with the frequencies, so that the W-channel is the noisiest. The instrumental resolution follows an opposite pattern, with the W channel having highest resolution (meaning the smallest instrumental beam). The V channel has the least contamination of foregrounds. Due to the frequency dependence of the foreground components, the Q channel is mostly contaminated by free-free and synchrotron radiation while in the W channel there is most radiation from dust. For our analysis we will often

use a noise-weighted average of the V and W channels, which we call the V + W channel.

For masking out foregrounds from the galaxy and point sources, we have mainly used the two masks released with the WMAP 5 year data. The KQ85 mask removes $\sim 18\%$ of the CMB sky, while the more conservative KQ75 mask removes $\sim 25\%$ of the sky.

The WMAP experiment has provided us with valuable knowledge about the nature of our universe. It has enabled us to estimate the CMB angular power spectrum with high precision (see fig 1.7). In combination with other experiments (measurements of the Hubble constant and the baryon acoustic oscillations) WMAP has tightly constrained the curvature of the universe and the equation of state parameter for dark energy, suggesting that we live in a flat universe with a cosmological constant. And not least, WMAP has provided us with robust knowledge about the contents and age of the universe [Komatsu et al. 2010].

Planck

No thesis on the topic of CMB is complete without mentioning European Space Agency's (ESA) current CMB mission: Planck. The Planck satellite was launched May 14 2009, and is expected to perform measurements of the CMB for approximately two years.

Planck will provide full-sky CMB temperature and polarization maps of significantly better resolution than WMAP. The satellite contains two instruments with different technology. The low frequency instrument (LFI) has radiometers covering three frequency channels, 30 GHz, 44 GHz and 70 GHz, with resolution in the range $56' - 14'$ FWHM. The high frequency instrument (HFI) uses an array of bolometers to cover six frequencies: 100 GHz, 143 GHz, 217 GHz, 353 GHz, 545 GHz and 857 GHz. These will deliver maps with a resolution of $9.5' - 5.0'$ FWHM. With these improved parameters, Planck defines the future of CMB analysis.

Chapter 2

Breaking the spell

2.1 Anomalies in the CMB

With all this data one can do more than just tune in the cosmological parameters to ever increasing precision. The CMB may be able to give us answers to very fundamental questions in cosmology. Or possibly raise questions we would else not think of.

As mentioned previously there exist many different models for inflation. The most commonly accepted being single field slow-roll inflation. Up until now it has been difficult to rule out or distinguish between models of inflation, since their observables are just barely within reach of the precision from observations. So far single field slow-roll inflation explains the problems described in section 1.1.2 and has not had any significant conflict with observations.

The single field slow-roll scenario predicts a universe which is flat, homogeneous and isotropic. This was the key motivations for introducing it in the first place. But it also predicts that the universe should be populated with adiabatic, scale invariant and nearly Gaussian perturbations. These are predictions we should test very thoroughly, since they may allow us to put constraints on inflation, and possibly rule out the models which are incorrect. As with all physics, a good model should be testable and be able to survive confrontation with data.

Several groups have searched for such kinds of anomalies in the CMB, but the difficulty is that deviations from isotropy, or Gaussianity does not take any specific form. It has in principle infinite degrees of freedom. So many different tests have been performed, and various anomalies have been found whose significance and possible origin are debated.

Some of the first anomalies that were found were some peculiarities at low multipoles of the CMB. First of all, the quadrupole of the CMB has an amplitude that is lower than expected. This is clearly visible on the CMB angular power spectrum (figure 1.7). This was discovered already in the COBE data [Bennett et al. 1992, Hinshaw et al. 1996]. However, since this is only a single multipole, and it is studied only after first seeing it in the data, it is difficult to award it a large significance.

Another large scale anomaly is the so called "axis of evil". When looking at the quadrupole and octopole it seems that most of the power for both of them is concentrated along a band around the sphere [Tegmark et al.(2003)]. What is more strange is that they are aligned along the same axis for both $\ell = 2$ and $\ell = 3$. In fact, there has been reports of unexpected features in multipoles up to $\ell \leq 6$ [Land & Magueijo 2005]. The significance and implications however, are still debated.

A different type of anomaly, present on many scales, is the hemispherical power asymmetry. The effect was was first noted in [Eriksen et al.(2004)], where the authors claim that the power is stronger on one hemisphere than the other, when separating along a certain axis. This means that the power spectrum has a different amplitude, depending on which part of the sky we are looking at. Several studies of this has been performed with the strongest significance of $3.5\sigma - 3.8\sigma$ claimed by [Hoftuft et al. 2009]. The origin of this anomaly is yet unknown.

Another strong anisotropy was detected by [Groeneboom & Eriksen 2009, Groeneboom et al. 2009], as predicted by a model proposed by [Ackerman et al. 2007]. The authors claim that the two-point function of the CMB contains a component which varies as a quadrupole on the sky, resulting in a preferred direction with a 9σ confidence. This anisotropy has passed several tests, but the indicated direction is pointing to the ecliptic poles, which also happens to be the spin axis of the WMAP satellite. This strongly suggests some kind of systematic effect. The WMAP team suggests that it is the result of incomplete handling of beam asymmetries [Bennett et al. 2010], but this has yet to be tested.

2.2 Searching for Non-Gaussianity

There are many alternative models of inflation, and testing for Gaussianity is one of the ways to distinguish between them. By a Gaussian CMB we mean that the spherical harmonic coefficients are described by a Gaussian distribution with variance of $\langle C_\ell \rangle$ (eq. 1.4). Different models predict different levels (and different types) of non-Gaussianity. For single field slow-roll inflation we expect only very small deviations from Gaussianity. An exciting aspect of this is that if we were to detect such a deviation from Gaussianity, we would be probing physics at a very high energy.

There are two main approaches for testing Gaussianity. We may perform a model independent test, or we may test a specific model for non-Gaussianity.

Model independent testing

In a model independent test we construct some kind of estimator, a variable or a function, θ, which we expect will depend on deviations from Gaussianity. This test should be performed both on the real data and on an ensemble of Gaussian simulations. By calculating θ for all the Gaussian simulations, we build a histogram

describing its distribution. This shows what values we should expect for θ in the Gaussian model,

Next, we estimate θ for the data, and compare the results with the distribution we found from simulations. From this we see precisely how typical the data are, under the assumption that the Gaussian model describes the data correctly. If they are very untypical, meaning that they are significantly different than the trend of the simulations, we are left with the following two possibilities.

Either it is just accidental. For this particular estimator our universe belongs to the tail of the distribution. We have only access to data from one universe, and for this particular estimator it might be unusual just by chance. It is important to have this possibility in mind. When we perform a large number of tests, this types of improbabilities will happen from time to time. Exactly how probable this is, we can find from the distribution of θ. If this deviation turns out to be very improbable, we might consider the second possibility.

The other alternative is that our model for making simulations do not correctly describe the data. It may be that our assumption of Gaussianity is incorrect. This could certainly explain why simulations and data are so different. Especially if our estimator is chosen to be sensitive to deviation from Gaussianity.

But there may be other reasons for our simulations to differ from the data. Especially, we should keep in mind foregrounds and systematic effects. In the simulations we assume that there are no foregrounds left in the map, while the data may contain remains of foregrounds, or undiscovered point sources. A first approach to test whether foregrounds are indeed responsible for the discrepancy between data and simulations is to perform the test on several individual frequency channels. Since foregrounds are frequency dependent, inconsistent results from these tests would be an indicator that foregrounds may be interfering.

This way of testing Gaussianity may have some advantages, depending on the estimator we choose. It may give an intuitive idea about what property in the map one is testing for (for example ellipticity in the spots). Also the estimator may sometimes be constructed so it is flexible, and allows us to look at separate scales or areas of the sky, or it may be computationally fast. However it is usually difficult to compare the results to theory. Also, it is difficult to compare the accuracy and results with that of different methods.

Model testing

The alternative to a model independent test is to make a model for quantifying non-Gaussianity, and then use the data to constrain a parameter. One such way is to constrain the non-Gaussianity parameter, f_{NL}. The primordial curvature perturbation field, $\Phi(\mathbf{x})$, at the end of inflation may be expanded around a Gaussian as follows:

$$\Phi(\mathbf{x}) = \Phi_L(\mathbf{x}) + f_{NL}\left(\Phi_L^2(\mathbf{x}) - \langle\Phi_L^2(\mathbf{x})\rangle\right)$$

where $\Phi_L(\mathbf{x})$ is the linear (Gaussian) part of the perturbation field[1].

Estimating a parameter, like f_{NL}, is more demanding than the model independent method, since we need to be able to make simulations with different nonzero values for this parameter. It is no longer enough to decide whether the Gaussian model is an acceptable description. We now need to find which value for f_{NL} best describes the data.

The advantage is that by estimating such a parameter, it is possible to compare models and data. Various models of inflation predict different values for f_{NL}. For single field slow-roll inflation $f_{NL} \sim 1$. Other inflationary scenarios (multiple scalar fields, curvaton inflation, inhomogeneous reheating just to mention a few) predict different values for f_{NL}, usually higher, depending on one or more free parameters in the model [Bartolo et al. 2004].

2.2.1 Constraining f_{NL}

In paper I and II in this thesis we have estimated deviation from Gaussianity by constraining the parameter f_{NL} introduced in the previous section. For this we combined two different tools, the bispectrum and needlets.

Bispectrum

The CMB bispectrum is a three point correlation function. It may be found as a correlation of spherical harmonic coefficients $\langle a_{\ell_1 m_1} a_{\ell_2 m_2} a_{\ell_3 m_3} \rangle$. If we assume statistical isotropy we get the angular averaged bispectrum, $B_{\ell_1 \ell_2 \ell_3}$ defined by

$$\langle a_{\ell_1 m_1} a_{\ell_2 m_2} a_{\ell_3 m_3} \rangle = \langle B_{\ell_1 \ell_2 \ell_3} \rangle \begin{pmatrix} \ell_1 & \ell_2 & \ell_3 \\ m_1 & m_2 & m_3 \end{pmatrix} \tag{2.1}$$

where the matrix represents the Wigner-3j symbol. $B_{\ell_1 \ell_2 \ell_3}$ is rotationally invariant, and if the harmonic coefficients $a_{\ell m}$ are Gaussian, the expectation value of $B_{\ell_1 \ell_2 \ell_3}$ is exactly zero.

The bispectrum of the CMB is an excellent estimator for non-Gaussianity. Since it is vanishing for a Gaussian sky, any significant signal will in principle be a non-Gaussian one. Unfortunately, calculating the bispectrum is a computationally demanding task. Since it is a three-point correlation function $B_{\ell_1 \ell_2 \ell_3}$ contains $\sim \ell_{max}^3$ elements. And if we want to consider scales up to, say $\ell_{max} \sim 1000$, the bispectrum contains 10^9 elements. Even with a considerable amount of symmetries this is costly to calculate, and a challenge to use for parameter estimation.

Another complication is the mask. Since the CMB map is contaminated with foregrounds it is absolutely necessary to remove this part from the analysis. But the mask disturbs the analysis significantly, since the spherical harmonic functions are no longer orthonormal. And in this way the bispectrum looses its sensitivity.

[1] In principle there is no need to stop after second order. $\Phi(\mathbf{x})$ may be expanded to any order. The coefficient of the third order term is usually called g_{NL} or τ_{NL}.

Needlets

A possible way to approach some of these difficulties with the bispectrum is to use wavelet transforms. Wavelet transforms are a general way of decomposing a function into localized base functions, called wavelets. By localized means that they have a non-zero value at the origin, and then approach zero asymptotically in all directions further away. As an example of a wavelet, figure 2.1 shows a needlet on the sphere. The wavelet usually defines a scale, given by a wavelet parameter.

By performing a wavelet transform, on a function, $T(\widehat{\gamma})$, (in our case a function on a sphere, the temperature map) we extract a representation of the function within the scales defined by the wavelet. This procedure is usually repeated for a number of different wavelet scales, resulting in a set of functions, each representing different scales of the original function, $T(\widehat{\gamma})$.

This is analogue to a spherical harmonic transform, $T \rightarrow a_{\ell m}$. The ℓ number defines the scale, in the same way as the wavelet scale. But instead of just having a number m representing the different directions on the sphere, wavelets have an entire map. The advantage of representing a function in this way is that it gives a great flexibility to study different scales and regions of a function separately.

Needlets are a new class of wavelets [Narcowich et al. (2006)]. They are the first type of proper wavelets defined on the sphere. This implies that the inverse needlet transformation is exact (no information loss). Also, needlets are localized in harmonic space, meaning that they cover a well defined interval of ℓ-scales, and are thus easy to compare with spherical harmonics. If not stated otherwise, the information in this section comes from [Marinucci et al. (2008)].

The spherical needlet function is defined as:

$$\psi_{jk}(\widehat{\gamma}) = \sqrt{\lambda_{jk}} \sum_{\ell} b\left(\frac{\ell}{B^j}\right) \sum_{m=-\ell}^{\ell} Y^*_{\ell m}(\widehat{\gamma}) Y_{\ell m}(\gamma_k) \tag{2.2}$$

where j denotes the needlet scale, λ_{jk} is a normalization factor, $\widehat{\gamma}$ is a direction on the sphere, and k is the pixel number in the coefficient map. $Y_{\ell m}(\widehat{\gamma}_k)$ are the spherical harmonic functions. The function $b\left(\frac{\ell}{B^j}\right)$ defines the weighting of the spherical harmonics. It is defined so that a given needlet scale, j, will be represented by spherical harmonics with scales $\ell \in [B^{j-1}, B^{j+1}]$. Outside this interval, $b\left(\frac{\ell}{B^j}\right) = 0$ (see [Marinucci et al. (2008)] for details).

When performing a needlet transform, the information from the map is expressed in the needlet coefficients β_{jk}, in the same way as the $a_{\ell m}$'s contain the information after a spherical harmonic transform. The needlet coefficients, β_{jk} are given as

$$\beta_{jk} = \int T(\widehat{\gamma}) \psi_{jk}(\widehat{\gamma}) \mathrm{d}\Omega \tag{2.3}$$

$$= \sqrt{\lambda_{jk}} \sum_{\ell m} b\left(\frac{\ell}{B^j}\right) a_{\ell m} Y_{\ell m}(\widehat{\gamma}_k) \tag{2.4}$$

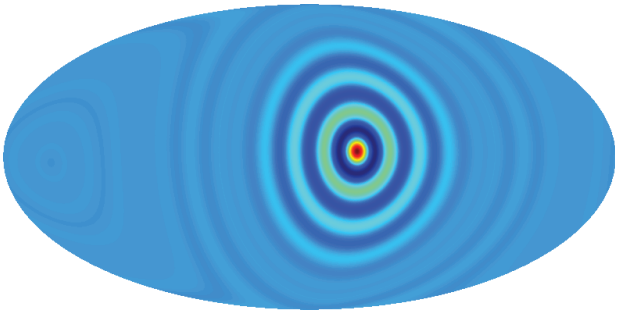

Figure 2.1: The shape of a needlet function. This is made by making a map on the sphere with a single nonzero pixel and then performing a needlet transform with $B = 1.205$, and looking at only the scale $j = 16$ (equivalent to $\ell \in [16, 24]$).

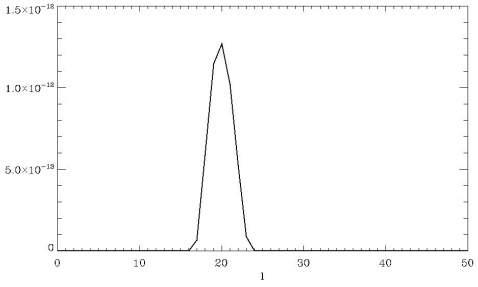

Figure 2.2: The power spectrum of the map in figure 2.1. Note that it is nonzero only for $\ell \in [16, 24]$.

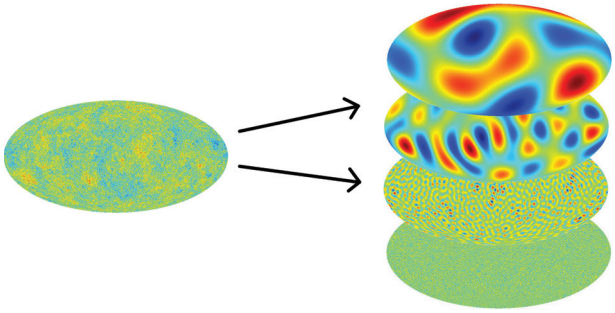

Figure 2.3: A needlet transform allows us to separate the map, into different scales.

From these, the original map may be found through the reconstruction formula:

$$T(\hat{\gamma}) = \sum_{j,k} \beta_{jk} \psi_{jk}(\hat{\gamma}) \tag{2.5}$$

In figure 2.1 a needlet transform has been performed on map with a single nonzero pixel. The figure displays the needlet coefficients, β_{jk}, for a given needlet scale, j, showing the shape of the needlet function. Figure 2.2 shows the power spectrum of the same map, demonstrating how the needlets are localized in harmonic space.

For the work presented in this thesis, the main advantage of using needlets is the localization property. In order to exclude foregrounds from the galaxy it is necessary to mask out a large region. As a result, the spherical harmonic functions are no longer orthogonal. More intuitively: Since the spherical harmonic functions are "periodic" around the sphere, the masked out region around the galaxy significantly affects the transform over the entire sphere. For needlets this is less of a problem. Since a needlet is localized, a mask like this will only influence needlet coefficients very close to the mask.

Another advantage of the localization property is that it allows for studying only selected parts of the sky. The wavelets in this region will almost exclusively be influenced by the structures there. We have taken advantage of this in Paper II, where we have performed an estimate of f_{NL} on separate regions on the sky.

Computing the bispectrum of needlets [Lan & Marinucci (2008)] is in some ways equivalent to computing the harmonic bispectrum from binned $a_{\ell m}$'s. But by using the needlet bispectrum instead of the normal bispectrum we avoid some of the problems mentioned in the previous section.

Since the each of the needlet scales contain the information from many ℓ-scales, the number of needlet scales that we need are much fewer. This greatly reduces the size of the needlet bispectrum as compared to the normal harmonic bispectrum,

and thus the computational cost is reduced. Also, the localization property of the needlets minimizes the difficulties with using a mask.

Constraining non-Gaussianity

In paper I and II we used the needlet bispectrum to estimate f_{NL}. We made use of 300 non-Gaussian simulated sets of $a_{\ell m}$'s generated using the algorithm developed in [Liguori et al (2003), Liguori et al. (2007)]. These were on the form

$$a_{\ell m} = a^G_{\ell m} + f_{NL} a^{NG}_{\ell m}. \tag{2.6}$$

We wanted to estimate which value for f_{NL} that best fits the data. We therefore used a χ^2 test for the comparing the data with the model. As always, the χ^2 value is found as:

$$\chi^2(f_{NL}) = \mathbf{d}^T(f_{NL})\mathbf{C}^{-1}\mathbf{d}(f_{NL}) \tag{2.7}$$

Where $\mathbf{C}$ is the covariance matrix and $\mathbf{d} = I^{obs}_{j_1 j_2 j_3} - \langle I_{j_1 j_2 j_3}(f_{NL})\rangle$. $I_{j_1 j_2 j_3}$ is here the needlet bispectrum [Lan & Marinucci (2008)]:

$$\begin{aligned} I_{j_1 j_2 j_3} &= \sum_k^{N_{pix}} \frac{\beta_{j_1 k}\beta_{j_2 k}\beta_{j_3 k}}{\sigma_{j_1 k}\sigma_{j_2 k}\sigma_{j_3 k}} \\ &= \sum_k \sum_{\ell_1\ell_2\ell_3} \sum_{m_1 m_2 m_3} \frac{b\left(\frac{\ell_1}{B^{j_1}}\right)}{\sigma_{j_1 k}} \frac{b\left(\frac{\ell_2}{B^{j_2}}\right)}{\sigma_{j_2 k}} \frac{b\left(\frac{\ell_3}{B^{j_3}}\right)}{\sigma_{j_3 k}} a_{\ell_1 m_1} a_{\ell_2 m_2} a_{\ell_3 m_3} \\ &\times\ Y_{\ell_1 m_1}(\widehat{\gamma}_k) Y_{\ell_2 m_2}(\widehat{\gamma}_k) Y_{\ell_3 m_3}(\widehat{\gamma}_k) \end{aligned} \tag{2.8}$$

The model we are testing in this case is represented by a specific value for f_{NL}. But since we want to find the value for f_{NL} which gives the best fit, we would have to repeat the test for many different values, and thus find the value for f_{NL} which results in the lowest χ^2.

But a much easier way is just to differentiate. The best fit, can be found as:

$$\frac{\mathrm{d}\chi^2(f_{NL})}{\mathrm{d}f_{NL}} = 0 \tag{2.9}$$

For this we need an explicit expression for $\langle I_{j_1 j_2 j_3}(f_{NL})\rangle$. By making use of eq. 2.6 we rewrite the three point correlation function of $a_{\ell m}$'s as:

$$\begin{aligned} &\langle a_{\ell_1 m_1} a_{\ell_2 m_2} a_{\ell_3 m_3}\rangle \\ =\ &\langle a^G_{\ell_1 m_1} a^G_{\ell_2 m_2} a^G_{\ell_3 m_3}\rangle + f_{NL}\big(\langle a^{NG}_{\ell_1 m_1} a^G_{\ell_2 m_2} a^G_{\ell_3 m_3}\rangle \\ +\ &\langle a^G_{\ell_1 m_1} a^{NG}_{\ell_2 m_2} a^G_{\ell_3 m_3}\rangle + \langle a^G_{\ell_1 m_1} a^G_{\ell_2 m_2} a^{NG}_{\ell_3 m_3}\rangle\big) \\ +\ &\mathcal{O}((a^{NG}_{\ell m})^2) \end{aligned} \tag{2.10}$$

We then neglect terms of higher than first order in $a^{NG}_{\ell m}$ (this factor is very small). The pure Gaussian term can also be neglected since the three point correlation function of a Gaussian field is zero. We use this result together with eq. 2.8 to find

$$\langle I_{j_1 j_2 j_3}(f_{NL})\rangle = f_{NL}\langle \hat{I}_{j_1 j_2 j_3}\rangle \tag{2.11}$$

where we have defined $\langle \hat{I}_{j_1 j_2 j_3} \rangle = \langle I^{NG,G,G}_{j_1 j_2 j_3} \rangle + \langle I^{G,NG,G}_{j_1 j_2 j_3} \rangle + \langle I^{G,G,NG}_{j_1 j_2 j_3} \rangle$. These three terms can be found from non-Gaussian simulations. Now we do not have to re-calculate $\langle I_{j_1 j_2 j_3}(f_{NL}) \rangle$ every time we want to test a new value for f_{NL}, we just need to find $\langle \hat{I}_{j_1 j_2 j_3} \rangle$ once.

Differentiating eq. 2.7, and using eqs. 2.9 and 2.11 we find an expression for the best fit f_{NL}:

$$f_{NL} = \frac{\langle \hat{I}_{j_1 j_2 j_3} \rangle^T \mathbf{C}^{-1} I^{obs}_{j_1 j_2 j_3}}{\langle \hat{I}_{j_1 j_2 j_3} \rangle^T \mathbf{C^{-1}} \langle \hat{I}_{j_1 j_2 j_3} \rangle} \tag{2.12}$$

where $I^{obs}_{j_1 j_2 j_3}$ is the needlet bispectrum of the map we want to test.

We can find $\mathbf{C}$ from Gaussian simulations, and $\langle \hat{I}_{j_1 j_2 j_3} \rangle$ from non-Gaussian simulations. We then use this to estimate f_{NL} on an ensemble of Gaussian simulations in order to quantify the error bars and possible bias of the estimate. Finally we estimate f_{NL} on the WMAP data.

In paper I we used this to estimate f_{NL} in the data and in simulations, resulting in constraints on the parameter. We explored the method, and performed a number of consistency checks.

In paper II we found that by using a higher value for the needlet parameter B we could obtain tighter constraints on f_{NL}. We also extended the analysis to study only selected regions of the sky. Since the needlets bispectrum can be expressed as a sum over pixels (eq. 2.8), it is then relatively unproblematic to sum over only the pixels we want to include in the estimate. We found constraints on f_{NL} using hemispheres and 45° discs in different directions. We also estimated f_{NL} using rings parallel to equator, in order to uncover possible foreground contamination outside the galactic mask.

The error bars on these estimates are naturally quite large, since much less data is being used for the analysis, as compared to a full-sky analysis. Still, this is the first attempt to estimate f_{NL} in different directions, and as the method and data improves it might be possible to constrain certain models predicting anisotropic f_{NL} (for example [Karciauskas et al. 2009]). However, maybe the most important use is to detect possible systematic effects and residual foregrounds in the CMB map.

We performed the analysis described above on the combined V + W channel as well as the individual Q, V and W channels. This resulted in a best fit value of $f_{NL} = 73 \pm 31$ (at the 1σ level) on the V+W channel using the conservative KQ75 mask. We found consistent results in the V and W channels, but the Q channel showed significant deviation, suggesting contamination from foregrounds.

The error bars on f_{NL} from the needlet bispectrum are significantly larger than the ones obtained by [Smith et al. (2009)]. The authors used an optimal bispectrum estimator to find $-4 < f_{NL} < 80$ at 95% CL which is the current best limits from CMB data. Still, the needlet bispectrum provides an important test of consistency.

The partial sky estimates yielded no significant local deviation from Gaussianity, with a possible exception of a 3σ deviation around the equatorial region in the Q channel, suggesting possible residual foregrounds outside the mask.

Also, we noted that in the V + W channel the estimates on all the equatorial rings show $f_{NL} > 0$. The probability for this to happen in a universe with $f_{NL} = 0$ is less than 1%.

In conclusion we found no significant anisotropy in the f_{NL} estimates in the CMB sky. We found no abnormal values for f_{NL} close to the galactic mask, with the exception of the Q channel, where we suspect influence from foregrounds.

2.2.2 Local Curvature

The local curvature is a conceptually simple and model independent approach to testing for non-Gaussianity in the CMB. The estimator is based on [Doré et al.(2003)] and consists of classifying pixels as hills, lakes or saddles based on their second derivatives.

The Hessian matrix is defined from the covariant second derivatives of the map, T:

$$H = \begin{bmatrix} \frac{\mathrm{D}^2 T}{\mathrm{D}\theta^2} & \frac{\mathrm{D}^2 T}{\mathrm{D}\theta \mathrm{D}\phi} \\ \frac{\mathrm{D}^2 T}{\mathrm{D}\theta \mathrm{D}\phi} & \frac{\mathrm{D}^2 T}{\mathrm{D}\phi^2} \end{bmatrix} \tag{2.13}$$

Here $\frac{\mathrm{D}T}{\mathrm{D}\theta}$ and $\frac{\mathrm{D}T}{\mathrm{D}\phi}$ indicates covariant derivatives. The two eigenvalues of this matrix may be found, and every pixel on the sphere may be classified as a hill, lake or saddle pixel depending on the signs of the eigenvalues.

A temperature threshold, T_t, is then introduced. For *only* the pixels with $T_i \geq T_t$ the fraction of hills, lakes and saddles are found. Then the threshold, T_t, is increased a small step and the analysis is repeated. This is done from a low T_t, where almost all pixels are included in the analysis, and up to a high T_t, where only a small portion of the map is included. The results are three functions, describing the fractions of hills, lakes and saddles as a function of T_t (figure 2.4).

As it happens, these functions are quite predictable for a Gaussian map. For this reason they are useful for testing for non-Gaussianity. However, since we do not completely trust the theoretical prediction of these curves, due to numerical issues with masks, derivatives and smoothing, we calibrate with simulations. An ensemble of Gaussian CMB skies are simulated, with instrumental beam and noise. For each of them the three functions are found, and we the calculate mean and standard deviation of these (and the covariance matrix). This corresponds to the Gaussian prediction.

Then we find the same three functions with the CMB data. And we are now able to decide whether the data behave similarly as the Gaussian simulations. For this comparison we again use a χ^2 test:

$$\chi^2 = \mathbf{d}^T \mathbf{C}^{-1} \mathbf{d}$$

where $\mathbf{C}$ is the covariance matrix and the data vector $\mathbf{d}$ contains the values of one (or several) of the curvature functions for a map (hill, lake or saddle fraction as a function of T_t), with the mean value subtracted. The map in question could be a simulation or it could be the real data.

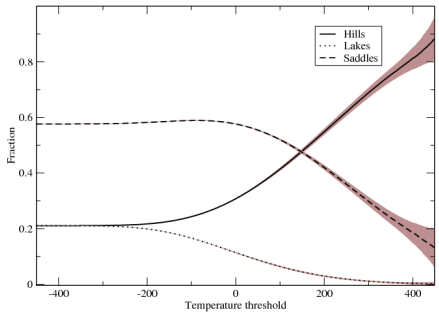

Figure 2.4: The fraction of hill, lake and saddle pixels in a simulated Gaussian map with $N_{side} = 512$. The simulation is generated from the best fit power spectrum from the WMAP 5 year release. The black line shows the mean, while the shaded area depicts the 68% confidence area.

The χ^2 value describes how well the tested data fits to a model. A low number means it fits well with the model (Gaussian), and a high number means it fits badly (non-Gaussian). We can now find this χ^2 number for another ensemble of simulations, and for the data, and we can see how well the data fits compared to the Gaussian simulations.

This test was first performed by [Hansen et al. 2004]. The authors found no significant deviation when considering the whole sky, but when looking separately on the northern and southern galactic hemisphere, deviations from Gaussianity was found on each part. They found that one of the hemispheres had an excess of hills while the other had too much lakes. On average however, the distribution was normal. They estimated this peculiar asymmetry on hemispheres along several different axises, and found a direction where the asymmetry was largest. This was close to the ecliptic axis.

However, in [Hansen et al. 2004] this analysis was performed on the WMAP first year data and with limited computational resources. In paper III we therefore performed the analysis on the WMAP 5-year data, having better control over the noise. Also we were able to use significantly more Gaussian simulations thus properly mapping out the χ^2 distribution.

Additionally, in [Hansen et al. 2004] only a diagonal covariance matrix was used, ignoring correlations between threshold levels. In Paper III we performed the test both with a diagonal covariance matrix and with a complete one, including correlations between threshold levels, T_t.

When using the full covariance matrix we found some evidence of a $\sim 1\%$ deviation from Gaussianity on scales areound 3°. When investigating the separate northern/southern galactic/ecliptic hemispheres as well as other scales, we found no deviation beyond 2σ. When investigating 48 different hemispheres around the

sky, we found no evidence for a preferred direction. We concluded that there is no evidence for non-Gaussianity or asymmetry in the WMAP data based on this test.

When using a strictly diagonal covariance matrix however, we found a detection more similar to the analysis in [Hansen et al. 2004]. Stronger hints of deviation from Gaussianity are found, and an axis of maximal asymmetry is estimated to be close to the ecliptic poles. The nature of this non-Gaussian detection when using diagonal covariance matrix is still unclear.

Chapter 3

Conclusions

In this thesis, through three papers I have presented two methods for estimating non-Gaussianity in the CMB. Both of these methods have been used to estimate non-Gaussianity in different directions on the sky, thus testing for anisotropic non-Gaussianity.

The method applied in paper III (described in section 2.2.2) is a model independent test, developed by [Doré et al.(2003)] and [Hansen et al. 2004], making use of local curvature statistics on the sphere. We have applied this test to newer data, making use of improved computational resources and we have explored the independent ecliptic and galactic hemispheres. When using a diagonal covariance matrix we find hints of non-Gaussianity consistent with [Hansen et al. 2004], but when including correlations in a full covariance matrix, these detections disappear.

Another method (described in section 2.2.1) is used to constrain the non-Gaussianity parameter f_{NL}. In paper I we develop the method for estimating f_{NL} by use of the bispectrum of a new type of wavelets, called needlets. We perform a number of consistency tests, and conclude with a 2σ deviation from Gaussianity. In paper II we tighten the error bars, and further develop the method to estimate f_{NL} in different regions on the sky. We find consistent results in the V and W channels suggesting non-Gaussianity at the 2σ level. However, we find the that the Q channel gives inconsistent results, with a noticeable deviation from Gaussianity in the galactic area. We therefore conclude that the Q channel is too contaminated with foregrounds to be reliable for non-Gaussianity studies.

These types of analysis are important, both to test the validity of the standard inflationary scenario, but also for uncovering residual foregrounds and systematic effects. As the methods for extracting information out of the CMB becomes more refined, it becomes increasingly important to have a good control of these effects.

It will be vital to apply these estimators to the future release of the Planck data in order to confirm or discard the various hints of deviation from Gaussianity encountered in this thesis. The Planck experiment will provide high resolution maps in many frequencies. With its different systematics it will provide an independent and hopefully conclusive test for both these and many other reported deviations

from Gaussianity and isotropy. If any of these anomalies are confirmed to have a cosmological origin, alternative models for inflation should seriously be considered.

Additionally, the Planck data is likely to also suffer from residual foreground contamination and various systematic effects. Estimators of directional non-Gaussianity, like the ones described in this thesis will be useful tools for dealing with these challenges.

References

[Ackerman et al. 2007] Ackerman, L., Carroll, S. M., & Wise, M. B. 2007, Phys. Rev. D, 75, 083502

[Bartolo et al. 2004] Bartolo, N., Komatsu, E., Matarrese, S., Riotto, A. 2004, Phys. Rept., 402, 103-266

[Bennett et al. 1992] Bennett, C. L., et al. 1992, ApJ, 396, L7

[Bennett et al. 1996] Bennett, C. L. and Banday, A. J. and Gorski, K. M. and Hinshaw, G. and Jackson, P. and Keegstra, P. and Kogut, A. and Smoot, G. F. and Wilkinson, D. T. and Wright, E. L. 1996, ApJ, 464, L1

[Bennett et al. 2003a] Bennett, C. L., et al. 2003a, ApJS, 148, 1

[Bennett et al. 2003b] Bennett, C. L., et al. 2003b, ApJS, 148, 97

[Bennett et al. 2010] Bennett, C. L., et al. 2010, arXiv:1001.4758v1

[Bertone et al. 2005] Bertone, G., Hooper, D., Silk, J. 2005, Phys. Rept. 405:279-390

[Dodelson 2003] "Modern Cosmology", Dodelson, S. 2003, Academic Press

[Doré et al.(2003)] Doré, O., Colombi, S., & Bouchet, F. R. 2003, MNRAS, 344, 905

[Eriksen et al.(2004)] Eriksen, H. K., Hansen, F. K., Banday, A. J., Górski, K. M. & Lilje, P. B. 2004, ApJ, 605, 14

[Hansen et al. 2004] Hansen, F. K., Cabella, P., Marinucci, D. & Vittorio, N. 2004, ApJ, 607, L67

[Hinshaw et al. 1996] Hinshaw, G., Banday, A. J., Bennett, C. L., Górski, K. M., Kogut, A., Smoot, G. F., & Wright, E. L. 1996, ApJ, 464, L17

[Hoftuft et al. 2009] Hoftuft, J., Eriksen, H. K., Banday, A. J., G´orski, K. M., Hansen, F. K., & Lilje, P. B. 2009, ApJ, 699, 985

[Groeneboom et al. 2009] Groeneboom, N. E., Ackerman, L., Kathrine Wehus, I., & Eriksen, H. K. 2009, arXiv:0911.0150

[Groeneboom & Eriksen 2009] Groeneboom, N. E. & Eriksen, H. K. 2009, ApJ, 690, 1807

[Górski et al. 2005] Górski, K. M., Hivon, E., Banday, A. J., Wandelt, B. D., Hansen, F. K., Reinecke, M., Bartelmann, M. 2005, ApJ 622, 759

[Guth et al (1981)] Guth, A. H, 1981, Phys. Rev. D, 347

[Hinshaw et al. 2009] Hinshaw G., et al. 2009, ApJS, 180, 225-245

[Karciauskas et al. 2009] Karciauskas, M., Dimopoulos, K., Lyth, D. H. 2009, Phys. Rev. D80:023509

[Komatsu et al. 2010] Komatsu, E. et al. 2010, arXiv:1001.4538

[Lan & Marinucci (2008)] Lan, X. & Marinucci, D. 2008, Electronic Journal of Statistics, Vol. 2, pp.332-367, arXiv:0802.4020

[Land & Magueijo 2005] Land, K., Magueijo, J. 2005, Phys. Rev. Lett, 95, 071301

[Larson et al. 2010] Larson, D. et al. 2010, arXiv:1001.4635

[Liguori et al (2003)] Liguori, M., Matarrese S. and Moscardini, L. , 2003, ApJ, 597, 57

[Liguori et al. (2007)] Liguori, M. et al. 2007, Phys. Rev. D, 76, 105016

[Maldacena (2003)] Maldacena, J. M. 2003, JHEP, 0305, 013

[Marinucci et al. (2008)] Marinucci, D., Pietrobon, D., Balbi, A., Baldi, P., Cabella, P., Kerkyacharian, G., Natoli, P., Picard, D., Vittorio, N., 2008, MNRAS, 383, 539

[Mather et al. 1994] Mather, J. C. et al. 1994, ApJ, 420:439

[Narcowich et al. (2006)] Narcowich, F.J., Petrushev, P. and Ward, J.D. 2006, SIAM Journal of Mathematical Analysis 38, 2, 574

[Perlmutter et al. 1999] S. Perlmutter et al 1999, ApJ, 517, 565

[Smith et al. (2009)] Smith, K. M., Senatore, L. & Zaldarriaga, M. 2009, arXiv:0901.2572

[Tegmark et al.(2003)] Tegmark, M., de Oliveira-Costa, A. & Hamilton, A. J. 2003, Phys. Rev. D, 68, 123523

Part II

Articles

I

Paper I

An Estimate of the Primordial Non-Gaussianity Parameter f_{NL} Using the Needlet Bispectrum

Rudjord, Øystein.; Hansen, Frode K.; Lan, Xiaohong;
Liguori, Michele; Marinucci, Domenico; Matarrese, Sabino
APJ, Volume 701, pp. 369-376 (2009).

Paper II

Directional Variations of the Non-Gaussiainity Parameter f_{NL}
Rudjord, Øystein.; Hansen, Frode K.; Lan, Xiaohong;
Liguori, Michele; Marinucci, Domenico; Matarrese, Sabino
APJ, Volume 708, pp. 1321-1325 (2010).

II

Paper III

Hemispherical Asymmetries in the Local Curvature of the 5-year WMAP Data
Rudjord, Øystein.; Groeneboom, Nicolaas E.; Hansen, Frode K.;
Marinucci, Domenico; Cabella, Paolo
Arxiv: astro-ph/1002.1811

III